Pharmacokinetic modelling for the simultaneous assessment of perfusion and ^{18}F-flutemetamol uptake in cerebral amyloid angiopathy using a reduced PET-MR acquisition time: Proof of concept

Giorgos Papanastasiou [a,*], Mark A. Rodrigues [b], Chengjia Wang [a], Kerstin Heurling [c], Christophe Lucatelli [a], Rustam Al-Shahi Salman [b], Joanna M. Wardlaw [a,b], Edwin J.R. van Beek [a], Gerard Thompson [a,b]

[a] *Edinburgh Imaging Facility, Queen's Medical Research Institute, The University of Edinburgh, 47 Little France Crescent, Edinburgh EH16 4TJ, UK*
[b] *Centre for Clinical Brain Sciences, The University of Edinburgh, Edinburgh, UK*
[c] *Antaros Medical, Mölndal, Sweden*

ARTICLE INFO

ABSTRACT

Purpose: Cerebral amyloid angiopathy (CAA) is a cerebral small vessel disease associated with perivascular β-amyloid deposition. CAA is also associated with strokes due to lobar intracerebral haemorrhage (ICH). ^{18}F-flutemetamol amyloid ligand PET may improve the early detection of CAA. We performed pharmacokinetic modelling using both full (0–30, 90–120 min) and reduced (30 min) ^{18}F-flutemetamol PET-MR acquisitions, to investigate regional cerebral perfusion and amyloid deposition in ICH patients.

Methods: Dynamic ^{18}F-flutemetamol PET-MR was performed in a pilot cohort of sixteen ICH participants; eight lobar ICH cases with probable CAA and eight deep ICH patients. A model-based input function (mIF) method was developed for compartmental modelling. mIF 1-tissue (1-TC) and 2-tissue (2-TC) compartmental modelling, reference tissue models and standardized uptake value ratios were assessed in the setting of probable CAA detection.

Results: The mIF 1-TC model detected perfusion deficits and ^{18}F-flutemetamol uptake in cases with probable CAA versus deep ICH patients, in both full and reduced PET acquisition time (all $P < 0.05$). In the reduced PET acquisition, mIF 1-TC modelling reached the highest sensitivity and specificity in detecting perfusion deficits (0.87, 0.77) and ^{18}F-flutemetamol uptake (0.83, 0.71) in cases with probable CAA. Overall, 52 and 48 out of the 64 brain areas with ^{18}F-flutemetamol-determined amyloid deposition showed reduced perfusion for 1-TC and 2-TC models, respectively.

Conclusion: Pharmacokinetic (1-TC) modelling using a 30 min PET-MR time frame detected impaired haemodynamics and increased amyloid load in probable CAA. Perfusion deficits and amyloid burden co-existed within cases with CAA, demonstrating a distinct imaging pattern which may have merit in elucidating the pathophysiological process of CAA.

List of non-standard abbreviations
pIF   population-based IF
mIF   model-based IF

1. Introduction

Cerebral amyloid angiopathy (CAA) is a cerebral small vessel disease characterised by the deposition of β-amyloid protein in cortical and leptomeningeal arterial walls, which is common in healthy elderly and in people with dementia (Neuropathology Group, 2001). CAA is usually associated with stroke that is due to lobar rather than deep intracerebral haemorrhage (ICH) (Samarasekera et al., 2012), being present in 58% of patients with lobar ICH (Rodrigues et al., 2018). The modified Boston criteria are the current *in vivo* reference standard for CAA diagnosis, which use the presence of multiple sites of macro-haemorrhage, microbleeds, and/or cortical superficial siderosis on susceptibility-weighted (SWI) magnetic resonance imaging (MRI) to categorise a patient as probable, possible or no CAA (Linn et al., 2010). However, haemorrhages may represent the late consequences of advanced CAA, therefore pa-

tients with mild CAA before haemorrhage occurs, may not be identified on MRI.

Recent studies showed that amyloid-positron emission tomography (PET) can differentiate probable CAA from healthy elderly and patients with deep ICH, which is generally due to hypertension (Charidimou et al., 2017, 2018). However, another study did not show a difference in amyloid-PET uptake between patients with probable CAA and healthy controls (Baron et al., 2014). Furthermore, as amyloid-PET detects both perivascular and parenchymal β-amyloid, it may reflect CAA and/or Alzheimer's disease (AD) (Charidimou et al., 2017, 2018). A recent study assessed a surrogate measure of cerebral perfusion using standardised uptake value ratios (SUVR) analysis from an early phase ^{11}C-Pittsburgh compound B (^{11}C-PiB) time frame, reporting reduced SUVR in participants with probable CAA against age-matched controls (Farid et al., 2015). The same study showed lower SUVR occipital/posterior cingulate ratios in participants with probable CAA against a small cohort of AD patients (Farid et al., 2015). There is no work comparing absolute cerebral perfusion in probable CAA against deep ICH patients. Whether any increases in the amyloid-PET uptake may be associated with cerebral perfusion differences in a distinct pattern in probable CAA, is also currently unknown.

[18]F-flutemetamol is among the newer longer-lived amyloid-PET ligands, which has recently gained regulatory approval for the assessment of β-amyloid protein in AD (Wolk et al., 2018; Zwan et al., 2017; Nelissen et al., 2009; Heurling et al., 2015). ^{18}F-flutemetamol PET may enable the early detection of perivascular β-amyloid in CAA, versus the current clinical standard MRI biomarkers (Samarasekera et al., 2012). Nelissen et al. were the first to perform fully quantitative analysis from PET-computed tomography (CT) ^{18}F-flutemetamol data in a small cohort of six patients, demonstrating significant correlations in tissue uptake estimates between a reversible 2-tissue compartmental (2-TC) model versus Logan graphical analysis (Nelissen et al., 2009). In a follow-up study, Heurling et al. showed strong correlations in tissue uptake estimates derived using reference tissue models and SUVR versus the 2-TC model (Heurling et al., 2015). For both studies, the applied scanning window for dynamic imaging was 0–90 min (Nelissen et al., 2009; Heurling et al., 2015). Minimising PET acquisition time for dynamic acquisitions would be clinically important, as it would reduce patient discomfort and increase scanner availability whilst maintaining quantitative accuracy. Beyond these studies assessing correlations in AD, the pharmacokinetics of ^{18}F-flutemetamol in the presence of CAA using PET-MRI have not been examined. In addition, it is unknown whether kinetic model estimates extracted from reduced PET acquisition time frames (< 90 min) can robustly detect CAA.

Fully quantitative compartmental models in PET allow for both perfusion and tracer uptake estimates, simultaneously in the tissue of interest (Gunn et al., 2001). However, compartmental modelling requires a continuous metabolite-corrected (arterial) plasma input function (IF), and to measure this, repeated arterial sampling is needed throughout PET imaging (Nelissen et al., 2009; Heurling et al., 2015; Gunn et al., 2001). Arterial sampling is an invasive, labour-intensive procedure that increases patient discomfort (Boellaard et al., 2001; Eriksson et al., 1995). To avoid arterial sampling, reference tissue compartmental models were developed which incorporate an indirect input function from a reference tissue devoid of tracer-specific receptors or accumulation of proteins (Lammertsma and Hume, 1996; Lammertsma et al., 1996). A metabolite corrected population-based IF (pIF) from another PET study involving the same tracer can also be used, although pIF methods commonly require a relatively large number of patient-derived IF inputs to obtain a representative input function (Zanotti-Fregonara et al., 2013; Rissanen et al., 2015). A model-derived IF (mIF) proposed by Cunningham et al. was based on adopting the basic 1-tissue (1-TC) model using kinetic information from a reference tissue, to yield an expression for a patient-specific IF (Cunningham et al., 1991). Although introduced in simulation studies analysing neurotransmitter kinetics (Morris et al., 2005; Normandin and Morris, 2008), this mIF has not been

examined in compartmental modelling of ^{18}F-flutemetamol clinical data.

In this work, we investigated whether perfusion deficits and ^{18}F-flutemetamol uptake are associated with probable CAA lobar ICH cases versus patients with deep ICH. To investigate whether this information can be extracted using a simplified PET protocol, we examined perfusion deficits and ^{18}F-flutemetamol uptake using both a full (consisted of two separate dynamic phases acquired at 0–30 min and 90–120 min post-injection, respectively) and a reduced (30 min) PET-MR acquisition time frame. In that context, we devised a mIF method to perform 1-TC and 2-TC compartmental modelling which was compared against reference tissue models and SUVR in the setting of differentiating probable CAA lobar ICH cases from patients with deep ICH.

2. Materials and methods

2.1. Population and study design

Sixteen patients with recent stroke due to ICH in the NHS Lothian Health Board region of Scotland were recruited for ^{18}F-flutemetamol PET-MR imaging from the ongoing LINCHPIN study, which is a community-based inception cohort study of adults with spontaneous ICH, resident in NHS Lothian (Rodrigues et al., 2018). All participants received ^{18}F-flutemetamol PET-MR imaging 6–12 months after ICH when stable. Cognitive assessments were performed for all participants prior to PET-MR imaging, using the mini mental state examination, the Montreal cognitive assessment and Addenbrooke's cognitive assessment tests.

Exclusion criteria included a known history of dementia, an ICH secondary to an underlying cause other than cerebral small vessel disease (e.g. underlying tumour, intracranial vascular malformation, venous thrombosis, prior trauma or haemorrhagic conversion of a cerebral infarct) and contraindications to MRI. The study was performed with the approval of the Scotland A Research Ethics Committee, in accordance with the Declaration of Helsinki and with the written informed consent of all patients. ^{18}F-flutemetamol was produced according to good manufacturing practice guidelines (EudraLex, volume 4) at the Edinburgh Imaging-QMRI radiochemistry laboratories of the University of Edinburgh, using a GE Healthcare PETtrace8 cyclotron.

2.2. PET-MR data acquisition

[18]F-flutemetamol brain PET-MR imaging was performed using a hybrid 3T mMR Biograph system (Siemens Medical Solutions, Erlangen, Germany). Dynamic PET acquisition started at the time of intravenous injection of a target dose of 185 MBq (184.2 ± 6.2 MBq) ^{18}F-flutemetamol and lasted for 30 min in 3D list mode (phase 1). A second period of 30 min PET data acquisition was repeated at 90 min post ^{18}F-flutemetamol injection to 120 min (phase 2).

Before the start of each PET phase (1 and 2), a separate MR attenuation correction map was acquired using the manufacturer's ultrashort echo time sequence. The following MRI sequences were performed during PET phase 1: 3D T_1-weighted, T_2-weighted, fluid-attenuated inversion recovery (FLAIR) and SWI sequences; PET phase 2: 3D T_1-weighted, T_2-weighted, FLAIR, T_2^*-weighted gradient recalled echo and diffusion tensor imaging. For the MR attenuation correction ultrashort echo time and the 3D T_1-weighted (used for image reconstruction and image processing respectively), the pulse sequence details were: repetition time/echo time 11.90 ms/2.46 ms, flip angle 10°, 192 × 192 matrix, 300 × 300 field-of-view, number of echoes 2; repetition time/echo time 2300 ms/2.98 ms, flip angle 9°, inversion time 1100 ms, 256 × 256 matrix, 256 × 256 field-of-view, respectively.

Dynamic ^{18}F-flutemetamol PET scans were reconstructed into 16 frames over phase 1 (4 × 30, 6 × 60, 4 × 180, 2 × 300 s) and 11 frames over phase 2 (5 × 60, 2 × 150, 4 × 300 s), using a Ordered Subsets Expectation Maximisation reconstruction algorithm with 3 iterations, 21

subsets, 127 axial slices, 344×344 matrix, $2.09 \times 2.09 \times 2.00$ mm pixels and 2 mm Gaussian filter, using the ultrashort echo time MR sequence for attenuation correction. The reconstruction included corrections for randoms, dead time and scatter. For PET phases 1 and 2, the voxel values of all frames were decay-corrected to the time of ^{18}F-flutemetamol administration.

2.3. Patient diagnosis

A neuroradiologist assessed the SWI MR data using the Syngo Via software (Siemens Medical Solutions, Erlangen, Germany) to categorise participants as probable CAA or no CAA as defined by the modified Boston criteria (Linn et al., 2010), masked to the clinical and ^{18}F-flutemetamol PET data. The size of ICH was measured using the Syngo Via software.

According to these criteria, patients with two or more haemorrhagic foci (macrohaemorrhage, microbleed or cortical superficial siderosis) restricted to lobar, cortical or cortical-subcortical regions, were classified as probable CAA. Patients with deep ICH (non-lobar haemorrhage in the modified Boston criteria), were classified as neither probable or possible CAA (no CAA) (Linn et al., 2010). This assessment was used as the reference standard technique to evaluate quantitative ^{18}F-flutemetamol data analysis.

2.4. Visual assessments from ^{18}F-flutemetamol PET-MR data

Two neuroradiologists (MR and GT) who had completed the Vizamyl^{TM} (^{18}F-flutemetamol) Electronic Training Programme independently, rated the ^{18}F-flutemetamol uptake on the decay corrected PET images of phase 2 (derived from the 90 to 120 min post-injection interval) fused to the participant's 3D T_1-weighted images, using the Syngo Via software. Scans were classified as ^{18}F-flutemetamol positive overall, if there was at least one positive region. In the absence of positive regions, scans were classified as negative. In the event of disagreement, the images were reviewed together and a consensus was reached. The consensus decision for overall positive/negative classification was used to determine ^{18}F-flutemetamol PET positivity/negativity.

2.5. Image analysis

To derive time-activity curves (TAC) and SUVR from the PET data across all brain regions, PET-MR co-registration and segmentation was performed using dedicated software (PMOD 3.8, Switzerland). Firstly, the 3D T_1-weighted MR data acquired in phases 1 and 2 were each spatially registered to a T_1-weighted Montreal Neurological Institute (MNI) brain template (via non-linear registration). The transformation matrix from the previous non-linear registration step was saved and then used to register (the dynamic and static) PET data to the registered (to the MNI template) 3D T_1-weighted data. Tissue probability maps were generated on the co-registered 3D T_1-weighted data based on the tissue probability map operation of SPM8 incorporated into PMOD (Ashburner and Friston, 2005), which were then used to extract TAC and SUVR from the cortical areas.

Based on the MNI template, standard volumes of interest (VOIs) were defined on the co-registered PET images using automated anatomical labelling in PMOD for 9 brain regions: the left and right frontal, parietal, temporal, occipital lobes, and the cerebellar cortex. Tissue quantification (perfusion-dependant and tracer uptake) comparisons were performed on TAC and SUVR extracted from the 8 cortical VOIs (target tissue) across all subjects. The cerebellar cortex TAC (reference tissue) extracted from each participant was used for the estimation of the mIF (in Eq. (5)) and as the reference tissue for the SRTM and FRTM analysis. Co-registration and VOI segmentation were performed separately in phases 1 and 2.

To interpolate regional brain uptake between phases 1 and 2, a bi-exponential function was fitted to all TAC in Matlab (MathWorks Inc.,
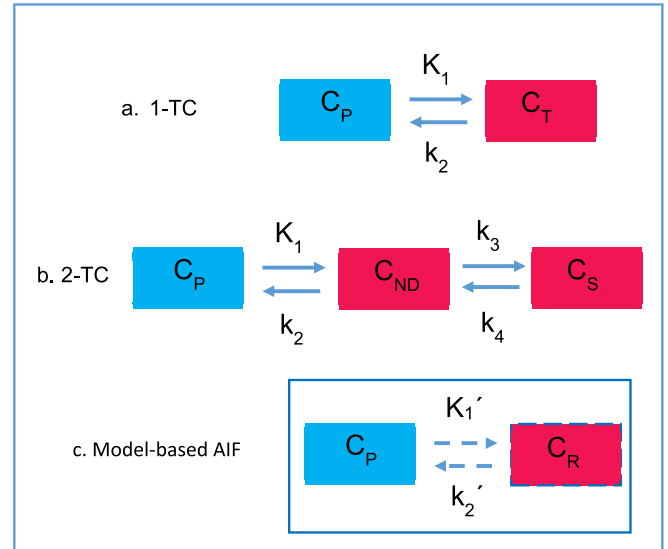
Fig. 1. (a) 1-tissue compartmental (1-TC) and (b) 2-tissue compartmental (2-TC) model illustrations. C_P, C_T, C_{ND} and C_S are the concentrations of non-metabolised tracer in the arterial plasma, total concentration of tracer in the tissue, non-displaceable tracer in tissue and specifically bound tracer in the tissue, respectively. K_1-k_4 are the rate constants. (c) Exchange of radioactivity concentration with rate constants K_1' and k_2', between the C_P and the concentration of tracer in the reference region (devoid of specific binding) C_R.

Natick, MA) as described by Nelissen et al. (2009):

$$Exponential\ function = \varphi_1 e^{-\theta_1 t} + \varphi_2 e^{-\theta_2 t} \qquad (1)$$

Note that the second term of Eq. (1) was allowed to tend to 0 (using the standard fittype Matlab function) when interpolation was approaching mono-exponential decays.

2.6. Model-based plasma input function

To measure an accurate metabolite-corrected IF required for 1-TC and 2-TC modelling in PET, arterial sampling is required to accurately measure arterial plasma radioactivity concentration (Gunn et al., 2001; Boellaard et al., 2001; Eriksson et al., 1995).

The 1-TC model can be described by (Fig. 1a):

$$dC_T(t)/dt = K_1 C_P(t) - k_2 C_T(t) \qquad (2)$$

where $C_P(t)$, $C_T(t)$ are the radioactivity concentrations from the arterial plasma and target tissue and K_1 (influx constant of tracer from arterial plasma into the tissue), k_2 (efflux constant of tracer from tissue into the arterial plasma), are the rate constants.

The 2-TC model can be described by the following set of equations (Fig. 1b):

$$dC_{ND}(t)/dt = K_1 C_P(t) - (k_2 + k_3)C_{ND}(t) + k_4 C_S(t)$$

$$dC_S(t)/dt = k_3 C_{ND}(t) - k_4 C_S(t) \qquad (3)$$

where $C_{ND}(t)$ and $C_S(t)$ are the radioactivity concentrations from the non-displaceable tracer and specifically bound tracer (separate compartments within the target tissue) and K_1-k_4 are the rate constants.

To avoid arterial sampling, reference tissue compartmental models were designed in which the arterial plasma IF $C_P(t)$ was substituted by an indirect IF (TAC) from a reference tissue region devoid of receptors that bind with the PET radiotracer (Lammertsma and Hume, 1996; Lammertsma et al., 1996).

The following relationship is satisfied and incorporated into the reference tissue compartmental models, describing the influx and efflux

of radioactivity concentration from the arterial plasma to the reference tissue (Fig. 1c):

$$dC_R(t)/dt = K_1'C_P(t) - k_2'C_R(t) \qquad (4)$$

where $C_R(t)$ is the radioactivity concentration from the reference tissue and K_1', k_2' are the rate constants. Solving Eq. (4) for C_R and by replacing the uptake rate constants K_1 and K_1' with their ratio R_1 (=K_1/K_1') to reduce the fitted parameters, C_P can be eliminated from the reference tissue compartmental modelling process, as previously described (Lammertsma and Hume, 1996; Lammertsma et al., 1996).

In our implementation, Eq. (4) can be re-written as (Cunningham et al., 1991):

$$C_P(t) = \frac{1}{K_1'}\left[\frac{dC_R(t)}{dt} + k_2'C_R(t)\right] \qquad (5)$$

Assuming that a) the PET radioactivity in the $C_R(t)$ represents the non-displaceable tracer in the cerebellar grey matter (reference tissue) region $C_R(t)$, b) there is no intermediate compartment between $C_P(t)$ and $C_R(t)$, and c) that ^{18}F-flutemetamol metabolites are polar molecules not able to cross the blood-brain-barrier (Normandin and Morris, 2008), the $C_P(t)$ can be modelled using Eq. (5).

In our mIF method, we used the TAC from the cerebellar grey matter region $C_R(t)$ of each patient, to derive an analytical expression for $C_P(t)$ per patient. To derive the derivative in Eq. (3), the $C_R(t)$ was differentiated with respect to time. In Eq. (5), the only unknown values were the influx and efflux constants K_1' and k_2'.

K_1' and k_2' were estimated by performing metabolite-corrected pIF-based 1-TC compartmental modelling (Fig. 1). The pIF was derived from a small cohort of six patients (Heurling et al., 2015). To avoid any bias in the per patient estimation of K_1' and k_2' that can be introduced by using a small cohort-derived pIF (Zanotti-Fregonara et al., 2013), pIF-based 1-TC-measured K_1' and k_2' across all patients were averaged and used as inputs in Eq. (5). It is important to note that the overall shape of the mIF is determined by the mean K_1' and k_2' values measured, the rate of change of $C_R(t)$ (estimated by the time derivative) and the $C_R(t)$ curve:

$$C_P(t) = f\left(\text{mean } K_1', \ \text{mean } k_2', \ \frac{dC_R(t)}{dt}, C_R(t)\right) \qquad (6)$$

This step allowed extraction of a metabolite free mIF per patient, which was used to evaluate the ability of 1-TC and 2-TC modelling in detecting probable CAA against deep ICH patients.

2.7. Quantitative analysis

Kinetic model analysis was performed using customised in-house software developed in Matlab. The code will be made available at (https://github.com/Georgerun/NeuroKinModel). The following steps were followed to measure mIF:

1 1-TC modelling was initially performed in the cerebellar cortex (used as the reference tissue) of all participants using a metabolite-corrected pIF derived from a small cohort of six patients: three healthy controls and three AD patients from a previous ^{18}F-flutemetamol PET study (Nelissen et al., 2009; Heurling et al., 2015). This step allowed to extract K_1' and k_2' estimates across all subjects.
2 To reduce any bias that can be introduced by using a small cohort-derived pIF, K_1' and k_2' estimates across all sixteen subjects were averaged and mean K_1' and mean k_2' were estimated.
3 Mean K_1' and k_2' values, the $C_R(t)$ curve from each subject (extracted from the cerebellar cortex VOI) and the rate of change of $C_R(t)$ (estimated by the time derivative) were then used in Eq. (5) to determine the mIF for each subject.

1-TC and 2-TC modelling was subsequently performed using the mIF estimated for each patient. Implementing mIF, 1-TC and 2-TC-derived

kinetic model estimates were assessed for their ability in detecting patients with probable CAA against patients with deep ICH, across 3 different PET acquisition time frames: a) an interpolated 120 min (phase 1 + 60 min interpolated phase + phase 2), b) concatenated 120 min (phase 1 + phase 2) and c) a 30 min (phase 1) PET acquisition. All TACs were also analysed using the simplified reference tissue model (SRTM) (Lammertsma and Hume, 1996) and the full reference tissue model (FRTM) (Lammertsma et al., 1996), across all 3 PET acquisition time frames. SUVR analysis was extracted from phase 2.

For each cortical VOI region, perfusion assessments were based on the uptake rate constant K_1 (in mL/min/mL of tissue; for input function compartment models) which describes the delivery of tracer from the arterial plasma to the brain and reflects cerebral perfusion, or the relative perfusion estimate R_1 (for reference tissue models) (Gunn et al., 2001). For all kinetic models, the k_2 estimate (min^{-1}) was also assessed and presented. The tracer specific binding was estimated either as the volume of distribution in each target region V_T (for 1-TC and 2-TC), or through the binding potential (BP_{ND}, as one of the fitted parameters in SRTM, or as the ratio of fitted parameters k_3/k_4 in FRTM models) (Heurling et al., 2015; Lammertsma and Hume, 1996; Koopman et al., 2018). For reference tissue modelling and SUVR, the cerebellar cortex was used as reference tissue throughout (Nelissen et al., 2009; Heurling et al., 2015; Lin et al., 2016; Hsiao et al., 2012; Rodriguez-Vieitez et al., 2016; Rostomian et al., 2011).

2.8. Statistical analysis

Dedicated software was used for statistical analysis (R Foundation for statistical computing, Vienna, Austria; MedCalc Software, Ostend, Belgium). Pearson correlation tests were performed to assess correlations and Bland Altman plot analysis was used to investigate systematic bias in kinetic model estimates, derived from reduced (30 min) against full interpolated and concatenated (0–30, 90–120 min) PET acquisition time frames. Box and whisker plots investigated differences in K_1 and V_T between cases with probable CAA and deep ICH patients. Statistical differences in perfusion-dependant (K_1, R_1), k_2 and tracer uptake (V_T, BP_{ND} and SUVR) estimates between probable CAA and deep ICH patients were assessed on a per cortical VOI region, using a two-sample unpaired t-test.

Receiver-operating characteristic (ROC) analysis was used to determine threshold values for 1-TC and 2-TC model-measured perfusion-dependant (K_1) and tracer uptake (V_T) estimates with the greatest sensitivity and specificity to detect probable CAA versus deep ICH (on a per cortical VOI region). A Delong et al. nonparametric comparison was used to compare the areas under the curve (AUC) of kinetic estimates derived from reduced against full (interpolated) PET acquisitions (DeLong et al., 1988). Model preference was assessed for the mIF 1-TC and 2-TC models (across all target tissue TACs) using the corrected Akaike Information Criterion (AICc). Statistical significance was defined as two-sided P value < 0.05.

3. Results

3.1. Participants

All baseline characteristics are presented in Table 1. In total, sixteen ICH participants underwent PET-MR imaging and analysis, eight lobar ICH cases with probable CAA and eight deep ICH patients with no CAA (Fig. 2) (Linn et al., 2010). All participants were independent before the ICH (modified Rankin scale 0 or 1) and presented with relatively small symptomatic ICH (the median ICH volume was 4 cm^3, with IQR 2–17).

Cases with probable CAA were slightly older compared with the deep ICH patients, although this difference did not reach statistical significance. Cognition assessments were performed for all participants prior to PET-MR imaging, to identify cases with probable CAA and patients with deep ICH with similar history of cognitive impairment, given that

Table 1

Baseline characteristics and visual assessments from the ^{18}F-flutemetamol data across all subjects.

Baseline characteristics		Lobar ICH with probable CAA cases (N = 8)	Deep ICH patients (N = 8)	P value (where applicable)
Age (years)		72 ± 8	68 ± 6	0.223
Sex m/f		4/4	6/2	0.334
ICH region		Lobar	Deep	
ICH location				
Basal ganglia			6	
Thalamus			2	
Frontal		3		
Occipital		2		
Parietal		1		
Temporal		2		
Hypertension		0	8	
Time between ICH and PET-MRI (days); median (IQR)		305 (240–350)		
Time between cognitive assessment and PET-MRI (days); median (IQR)		41 (11–54)		
MMSE; median (IQR)		30 (29–30)	30 (30–30)	0.850
MoCA; median (IQR)		28 (27–28)	26 (25–26)	0.084
ACEIII; median (IQR)		97 (94–98)	95 (93–95)	0.139
Visual assessment of the	Positive	7	0	<0.001
^{18}F-flutemetamol data	Negative	1	8	

ICH: intracerebral haemorrhage, IQR: interquartile range, MMSE = mini mental state examination, MoCA = Montreal cognitive assessment, ACEIII = Addenbrooke's cognitive examination.
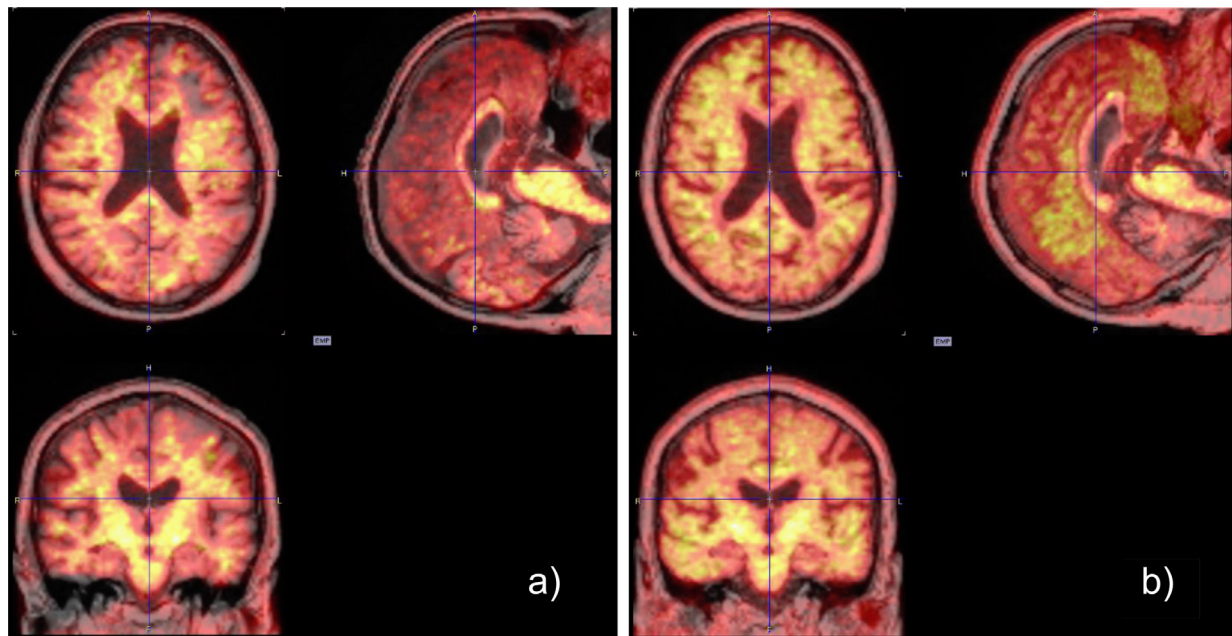
Fig. 2. Fused PET-MR images (static: 90–120 min) of ^{18}F-flutemetamol uptake from a patient with deep ICH (a) and a patient with probable CAA (b). ICH: intracerebral haemorrhage, CAA: cerebral amyloid angiopathy.

this can be a confounder of the association between CAA and stroke (Wolk et al., 2009). On cognition assessments, there were no significant differences between cases with probable CAA and patients with deep ICH (Table 1). All participants demonstrated normal cognitive functions (Table 1) (Wolk et al., 2009; Klunk et al., 2004).

On visual assessments, 7 out 8 cases with probable CAA were classified as positive and all patients with deep ICH were classified as negative for ^{18}F-flutemetamol uptake.

3.2. Quantitative analysis from full PET-MR acquisition

In total, 128 target tissue TACs were analysed (64 TACs from cases with probable CAA against 64 TACs from patients with deep ICH). Initially, 1-TC and 2-TC modelling was performed using the pIF from the full interpolated (0–30, 90–120 min) PET-MR data (mean values are presented in the Supplementary file 1). The whole blood and metabolite corrected pIF are illustrated in the Supplementary file 2. Significant differences between cases with probable CAA and patients with deep ICH were only observed for the K_1 estimate for both models ($P < 0.01$). No significant differences were observed in $K_1\prime$ and $k_2\prime$ estimates between 1-TC and 2-TC modelling, and between cases with probable CAA and patients with deep ICH for both models. The mean pIF 1-TC model-derived $K_1\prime$ and $k_2\prime$ estimates used to calculate the mIF are shown in the Supplementary file 1.

Subsequently, 1-TC and 2-TC modelling was examined using the mIF from the full interpolated (0–30, 90–120 min) PET-MR data. Examples of cerebellar cortex TACs and mIFs are presented in Fig. 3. The K_1 and k_2 estimates were significantly lower for both models in probable CAA
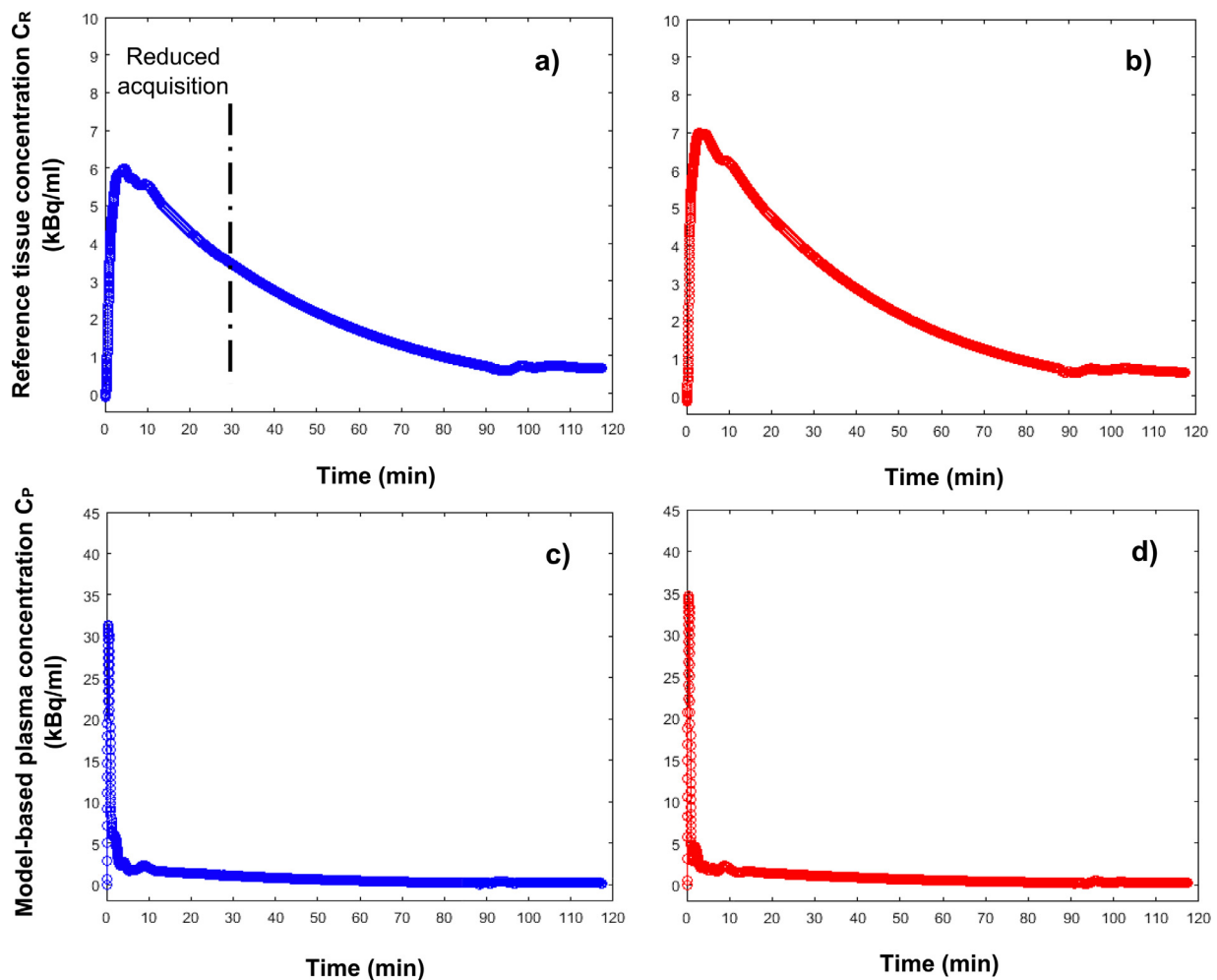
Fig. 3. Reference tissue (cerebellar grey matter) time-activity curves in (a) and (b) were used to estimate model-based input functions for the same control (c) and patient with probable CAA (d), respectively. Dash-dotted line in (a) shows the reduced PET acquisition time frame (30 min) of dynamic curves examined throughout.

cases against patients with deep ICH. The 1-TC-derived V_T was significantly higher in probable CAA cases versus patients with deep ICH (Table 2). Examples of 1-TC and 2-TC model fits are shown in the Supplementary file 3.

On box and whisker plots, the median and interquartile range (IQR) values for 1-TC and 2-TC-derived K_1 in cases with probable CAA and deep ICH patients were 0.24 (0.22, 0.27) and 0.27 (0.25, 0.30); 0.25 (0.23, 0.27) and 0.28 (0.25, 0.31), respectively (Fig. 4). The median and IQR values for 1-TC and 2-TC-derived V_T in cases with probable CAA and deep ICH patients were 2.88 (2.72, 3.08) and 2.74 (2.63, 2.88); 3.10 (2.87, 3.48) and 3.12 (2.87, 3.43), respectively (Fig. 4).

SRTM and FRTM models were also investigated using the full interpolated (0–30, 90–120 min) data. Significant differences between cases with probable CAA and patients with deep ICH were only observed for the R_1 and for the SRTM-derived k_2 estimates (Table 2).

To investigate whether the interpolated data can affect model estimates, kinetic modelling was repeated using full concatenated (eliminating interpolation) PET-MR data. Although significant differences between cases with probable CAA versus patients with deep ICH were maintained in the full concatenated analysis, these were lower compared to the full interpolated analysis across all models (Table 2).

SUVR analysis extracted from phase 2 was significantly higher in cases with probable CAA versus patients with deep ICH (mean SUVR=1.51±0.26 vs 1.26±0.16, respectively).

3.3. Quantitative analysis from reduced PET-MR acquisition

Following full interpolated and concatenated PET-MR analysis, quantitative analysis was investigated using a reduced (30 min; from phase 1) acquisition time frame. Both the mIF 1-TC and 2-TC models demonstrated significantly lower K_1 and k_2 estimates, and significantly higher tracer uptake (V_T) estimates for probable CAA cases versus deep ICH patients, respectively (Table 2). For the reference tissue models, significant differences between probable CAA cases and deep ICH patients were only observed for the R_1 and for the SRTM-derived k_2 estimates.

Correlations coefficients were investigated between kinetic model analysis derived from the reduced against full interpolated and concatenated PET-MR time frames (Supplementary file 4). All mIF and reference tissue models demonstrated significant, strong correlations in perfusion-dependant estimates derived from the reduced against full interpolated data (Fig. 5). Significant, strong correlations in tracer uptake estimates from reduced against full interpolated data were only observed for the case of the 1-TC model (Fig. 6). On Bland Altman plot analysis, the systematic bias between reduced against full PET-MR analyses were low, except for the 2-TC and FRTM-measured tracer uptake estimates (Fig. 6, Supplementary file 4).

On box and whisker plots, the median and IQR values for 1-TC and 2-TC-derived K_1 in cases with probable CAA and deep ICH patients were 0.25 (0.23, 0.26) and 0.28 (0.25, 0.31); 0.25 (0.23, 0.27) and 0.28 (0.26, 0.31), respectively (Fig. 4). The median and IQR values for 1-TC and 2-

Table 2

Mean (SD) kinetic model estimates measured using the model-based input function (mIF) and reference tissue models, across all PET acquisition time frames examined. Perfusion (K_1 or R_1), k_2 and tracer uptake estimates (V_T or BP_{ND}) for 1-TC, 2-TC, SRTM, FRTM models are presented, extracted from the 8 cortical VOIs (target tissue) across all subjects. The 8 cortical VOIs were the left and right frontal, parietal, temporal, occipital lobes (described in the Methods). Significant differences between cases with CAA and patients with deep ICH are denoted with *, ** and † (*, ** and † show $P < 0.05$, $P < 0.01$ and $P < 0.001$, respectively). K_1 and V_T are measured in mL/min/mL and mL/mL, respectively; R_1, and BP_{ND} are unitless quantities. The k_2 is measured in min^{-1}.

Acquisition frame/Model application 120 min PET (interpolated dataset)		mIF 1-TC	mIF 2-TC	SRTM	FRTM
K_1/R_1	Probable CAA	0.25 (0.03)†	0.26 (0.03)†	0.91 (0.08)†	0.89 (0.07)†
	Deep ICH	0.29 (0.03)†	0.29 (0.03)†	1.00 (0.14)†	1.00 (0.14)†
k_2	Probable CAA	0.09 (0.01)**	0.10 (0.01)**	0.05 (0.05)**	0.01 (0.04)
	Deep ICH	0.10 (0.01)**	0.11 (0.01)**	0.06 (0.08)**	0.03 (0.06)
V_T/BP_{ND}	Probable CAA	2.89 (0.30)**	3.19 (0.48)	0.25 (0.35)	0.34 (0.67)
	Deep ICH	2.73 (0.16)**	3.16 (0.49)	0.24 (0.44)	0.33 (0.45)
120 min PET (concatenated dataset)					
K_1/R_1	Probable CAA	0.29 (0.03)*	0.30 (0.03)*	0.93 (0.06)*	0.92 (0.06)*
	Deep ICH	0.32 (0.03)*	0.32 (0.03)*	0.98 (0.08)*	0.99 (0.11)*
k_2	Probable CAA	0.12 (0.01)*	0.12 (0.01)*	0.07 (0.09)*	0.03 (0.08)
	Deep ICH	0.13 (0.01)*	0.13 (0.01)*	0.14 (0.19)*	0.03 (0.08)
V_T/BP_{ND}	Probable CAA	2.42 (0.16)*	2.41 (0.15)	0.24 (0.40)	0.47 (0.66)
	Deep ICH	2.35 (0.15)*	2.37 (0.15)	0.23 (0.32)	0.45 (0.46)
30 min PET					
K_1/R_1	Probable CAA	0.25 (0.02)†	0.26 (0.02)†	0.93 (0.15)†	0.89 (0.08)†
	Deep ICH	0.30 (0.03)†	0.29 (0.03)†	0.99 (0.14)†	0.98 (0.11)†
k_2	Probable CAA	0.09 (0.01)**	0.09 (0.01)**	0.07 (0.09)**	0.02 (0.04)
	Deep ICH	0.10 (0.01)**	0.10 (0.01)**	0.11 (0.19)**	0.03 (0.05)
V_T/BP_{ND}	Probable CAA	2.84 (0.24)**	2.85 (0.34)**	0.26 (0.45)	0.43 (0.56)
	Deep ICH	2.63 (0.16)**	2.72 (0.20)**	0.25 (0.46)	0.42 (0.59)

ICH: intracerebral haemorrhage, SD: standard deviation, 1-TC: 1-tissue compartmental model, 2-TC: 2-tissue compartmental model, SRTM: simplified reference tissue model, FRTM: full reference tissue model, VT: volume of distribution, BPND: binding potential.
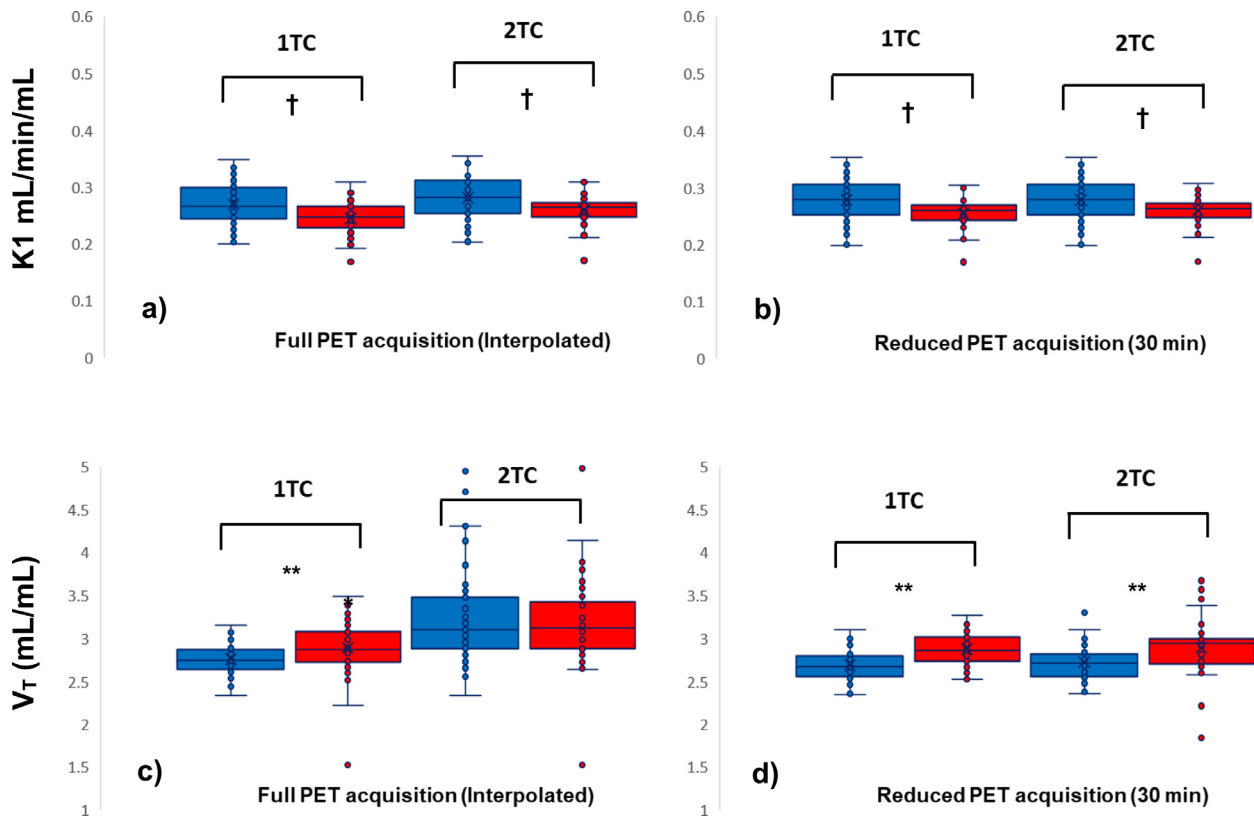
Fig. 4. Box and whisker plots demonstrating differences in K_1 (a, b) and V_T (c, d) estimates between cases with CAA (red) and patients with deep ICH (blue), for model-based input function 1-TC and 2-TC modelling. Model analysis from reduced (30 min) versus interpolated full (120 min) PET acquisition is shown. Significant differences between cases with CAA and controls for each model are denoted with ** (when $P < 0.01$) and † (when $P < 0.001$). CAA: cerebral amyloid angiopathy, 1-TC: 1-tissue compartment model, 2-TC: 2-tissue compartment model, ICH: intracerebral haemorrhage.
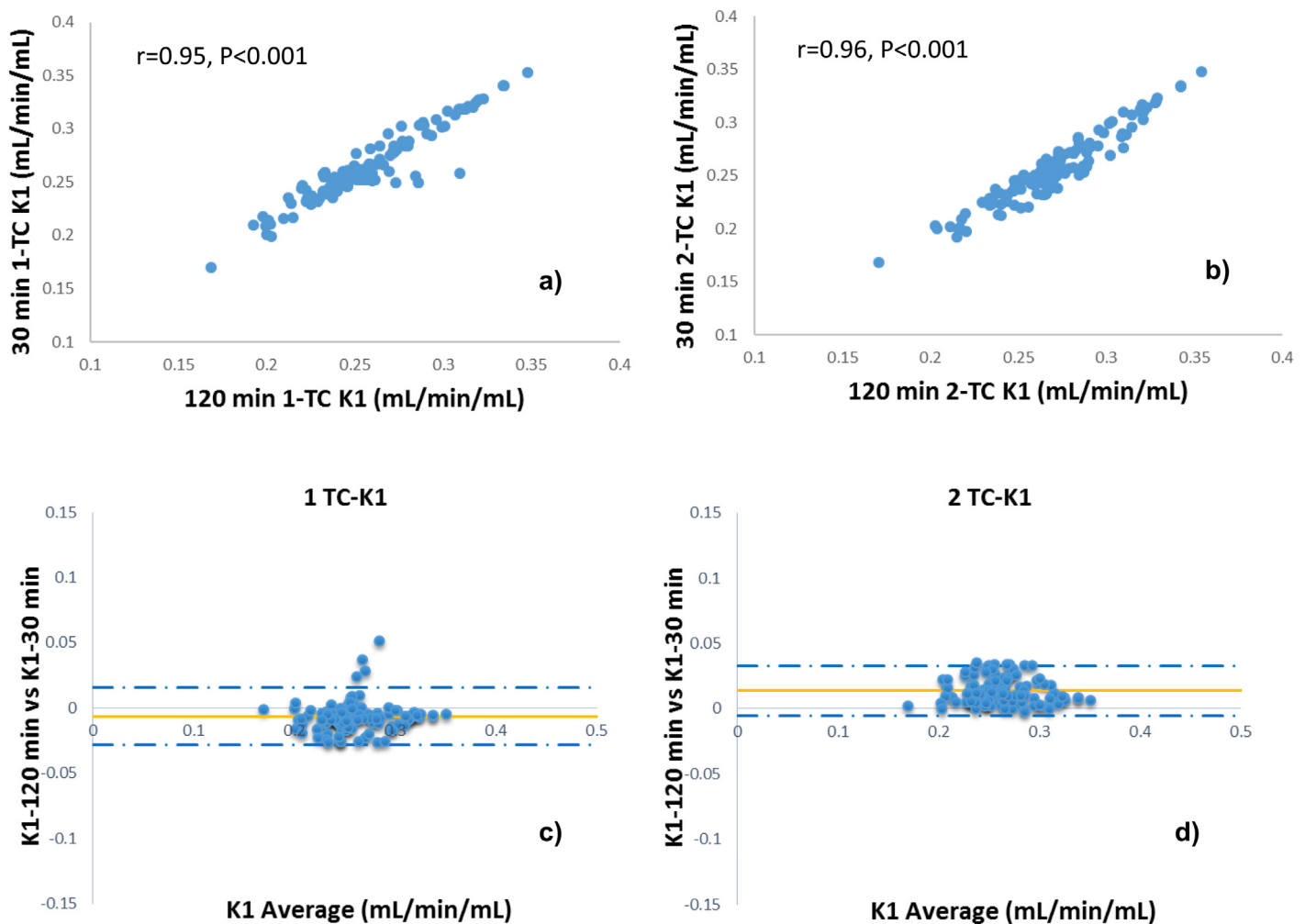
Fig. 5. Scatter plots with correlation coefficients (a, b) and Bland Altman plots (c, d) for 1-TC and 2-TC model-derived perfusion-dependant estimate K_1, in reduced versus full interpolated PET acquisition. 1-TC: 1-tissue compartment, 2-TC: 2-tissue compartment.

Table 3

Results from ROC analysis are presented. Parentheses show (95% confidence intervals). Statistically significant areas under the curve are shown with ** and † (** and † show $P < 0.01$ and $P < 0.001$, respectively). K_1 and V_T are measured in mL/min/mL and mL/mL, respectively.

Statistical analysis/Model	1-tissue compartment Reduced (30 min)	Full IN (120 min)	2-tissue compartment Reduced (30 min)	Full IN (120 min)
Areas under the Curve (AUC)				
K_1	0.87 (0.80, 0.93)†	0.88 (0.81, 0.95)†	0.83 (0.75, 0.91)†	0.81 (0.72, 0.90)†
V_T	0.84 (0.77, 0.91)**	0.84 (0.76, 0.92)**	0.76 (0.66, 0.86)**	0.54 (0.43, 0.65)
Thresholds on ROC analysis				
K_1	<0.26	<0.26	<0.27	<0.29
V_T	>2.62	>2.73	>2.75	>3.06
Sensitivity and Specificity				
Sensitivity (K_1)	0.87 (0.79, 0.95)	0.78 (0.68, 0.88)	0.85 (0.73, 0.97)	0.89 (0.78, 1.00)
Specificity (K_1)	0.77 (0.64, 0.87)	0.81 (0.72, 0.90)	0.64 (0.53, 0.75)	0.67 (0.55, 0.79)
Sensitivity (V_T)	0.83 (0.74, 0.92)	0.80 (0.69, 0.91)	0.83 (0.74, 0.92)	0.74 (0.60, 0.88)
Specificity (V_T)	0.71 (0.59, 0.83)	0.73 (0.61, 0.85)	0.63 (0.50, 0.76)	0.48 (0.32, 0.64)

VT: volume of distribution.

TC-derived V_T in cases with probable CAA and deep ICH patients were 2.86 (2.73, 3.02) and 2.67 (2.55, 2.80); 2.93 (2.69, 3.00) and 2.71 (2.56, 2.82), respectively (Fig. 4).

On ROC analysis, high AUC were observed for both mIF compartmental model-measured K_1 and tracer uptake estimates (Table 3, Fig. 7). The highest AUC for the detection of probable CAA cases against deep ICH patients was reached by the 1-TC model, across both the reduced and full interpolated PET-MR data analysis ($P < 0.01$). There was a sig-

nificant improvement in the AUC for the 2-TC-measured V_T extracted from the reduced time frame against full interpolated PET-MR data analysis. No other differences in AUC were observed between the reduced and full interpolated time frames.

High concurrence of perfusion deficits and amyloid burden was observed for both 1-TC and 2-TC models, in the reduced time data analysis (Table 4, Fig. 7). Overall, 52 and 48 out of the 64 brain areas with amyloid deposition (V_T>thresholds identified on ROC; Table 3) showed
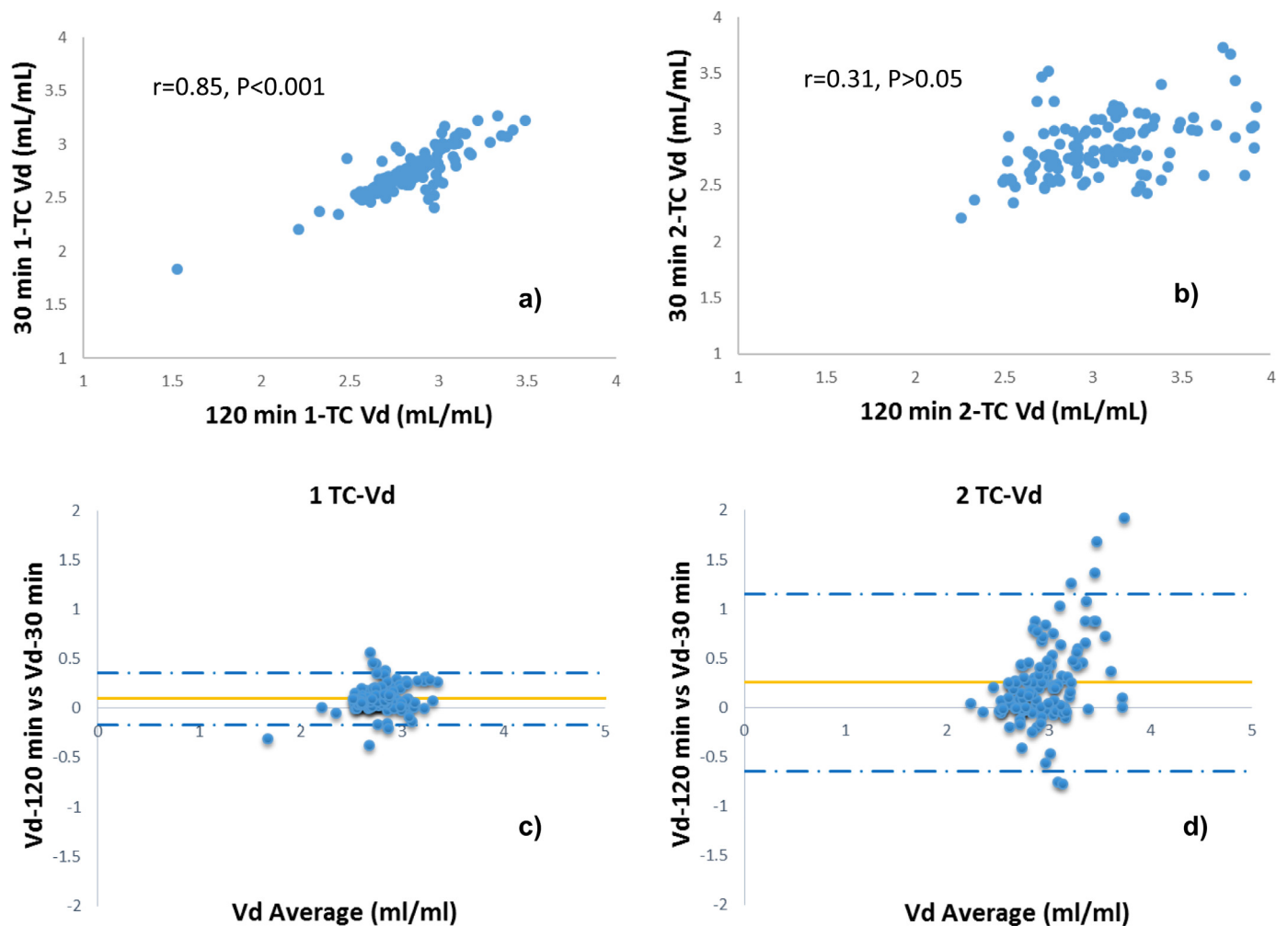
Fig. 6. Scatter plots with correlation coefficients (a, b) and Bland Altman plots (c, d) for 1-TC and 2-TC model-derived volume of distribution V_T, in reduced versus full interpolated PET acquisition.

Table 4

Co-occurrence of cerebral perfusion deficits in areas of increased amyloid load for patients with probable CAA and patients with deep ICH, per brain region ($N = 16$ per brain region, e.g. left and right frontal times 8 patients) and total ($N = 64$, for all brain regions across all lobes) per group (8 cases with probable CAA; 8 patients with deep ICH). Co-occurrence of perfusion deficits and amyloid burden was defined as both K_1 and V_T estimates being lower and higher than ROC-identified thresholds for K_1 and V_T (see Table 3) within a brain region, respectively.

Model and PET-MR time frame/brain region ($N = 16$) and total ($N = 64$)	1-TC (30 min)	2-TC (30 min)	1-TC (120 min)	2-TC (120 min)
Frontal- CAA	13	12	13	10
Occipital- CAA	12	11	12	12
Parietal- CAA	14	12	13	10
Temporal- CAA	13	13	13	10
Total- CAA	52	48	51	42
Frontal- deep ICH	0	1	1	2
Occipital- deep ICH	0	0	2	4
Parietal- deep ICH	1	2	1	2
Temporal- deep ICH	3	4	4	4
Total- deep ICH	4	7	8	12

ICH: intracerebral haemorrhage, 1-TC: 1-tissue compartmental model, 2-TC: 2-tissue compartmental model. The full interpolated (120 min) PET-MR time frame was assessed.

reduced perfusion ($K_1 <$thresholds identified on ROC) for 1-TC and 2-TC models, respectively. This was also observed for the 1-TC model in the full interpolated data analysis. Using the reduced PET-MR time frame in the full cohort, K_1 estimates in brain areas with amyloid burden were significantly lower compared to areas without amyloid load ($P < 0.005$, for both models).

3.4. Quality of model fit

On AICc, all brain regions showed a marginal preference for 1-TC versus 2-TC in the full interpolated PET (frontal: 53%, parietal: 52%, temporal: 51%, occipital: 55%, in supplementary file 5). All regions showed slightly stronger preference for 1-TC versus 2-TC in the reduced
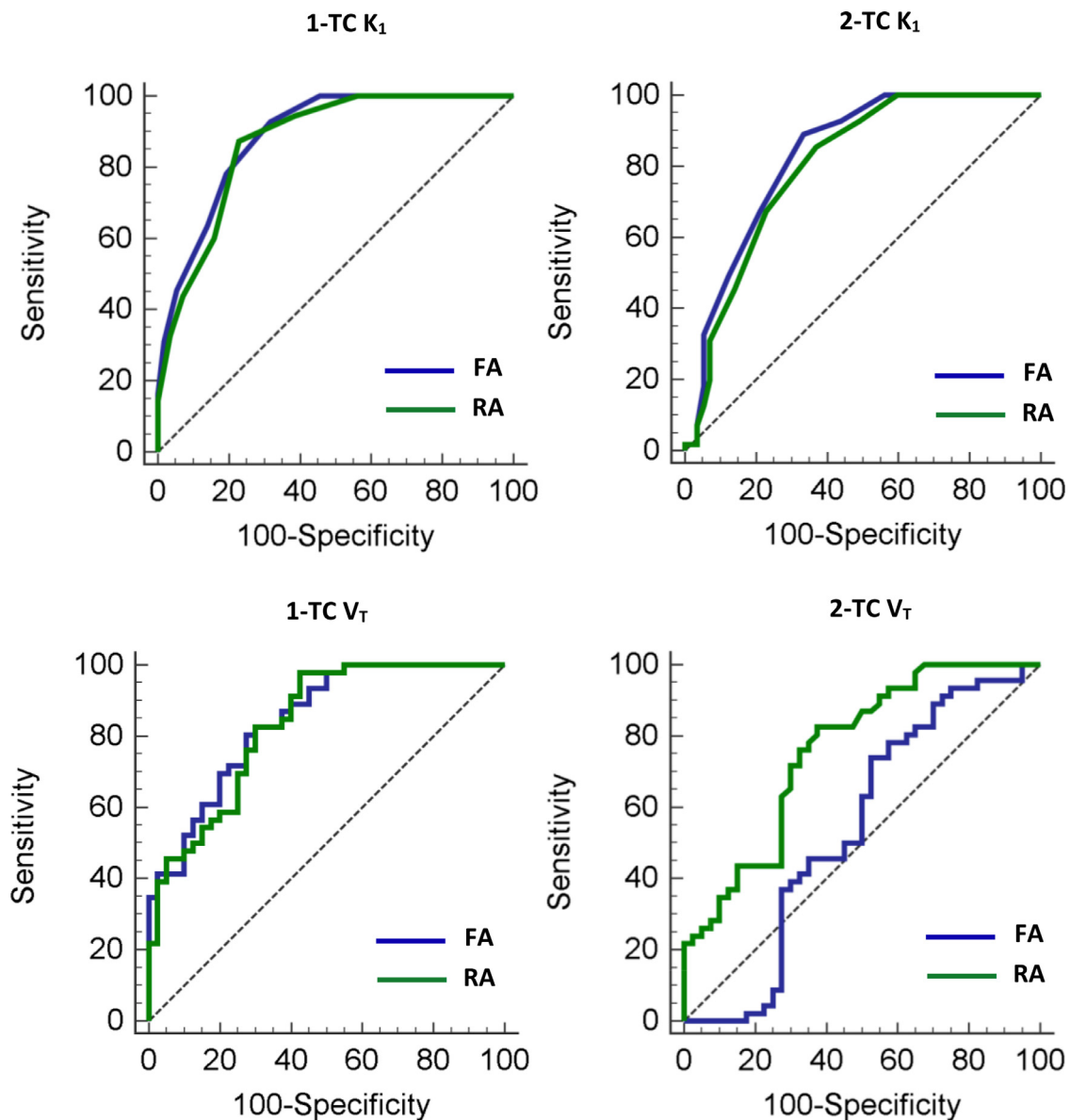
Fig. 7. ROC curves presenting sensitivity and specificity of mIF 1-TC and 2-TC modelling from reduced (RA-30 min; green line) versus full interpolated (FA-120 min; blue line) PET acquisition, in terms of identifying cases with probable CAA versus patients with deep ICH (and no CAA) classified using the modified Boston criteria. mIF: model-based input function, 1-TC: 1-tissue compartment, 2-TC: 2-tissue compartment, CAA: cerebral amyloid angiopathy, ICH: intracerebral haemorrhage.

(frontal: 58%, parietal: 53%, temporal: 57%, occipital: 56%, in supplementary file 5) against the full interpolated PET, although this difference between models remained small.

On visual inspection, no obvious differences were observed between 1-TC and 2-TC model fits and both models were able to fit appropriately the peak and the tail of all TAC.

4. Discussion

The main findings of this study demonstrated that PET compartmental modelling reached high sensitivity and specificity for differentiating lobar ICH participants with probable CAA from deep ICH patients (classified using the modified Boston criteria) in a pilot cohort. Using the mIF method in ^{18}F-flutemetamol PET-MR data, the 1-TC model identified congruent perfusion impairments and amyloid accumulation in participants with probable CAA against patients with deep ICH, which were consistent in both the reduced versus the full interpolated PET-MR data analysis.

4.1. Cases with probable CAA against patients with deep ICH

This is the first study assessing the sensitivity and specificity of compartmental models using a kinetic model-based input function method from dynamic PET-MR data, for the detection of probable CAA. We showed that mIF 1-TC modelling consistently detected perfusion deficits and amyloid deposition in cases with probable CAA against patients with deep ICH. This is an important step towards rigorously investigating whether perivascular β-amyloid is a distinct underlying pathology leading to stroke due to ICH, versus hypertension-associated presumed arteriosclerosis and deep ICH (Group, 2001; Samarasekera et al., 2012; Rodrigues et al., 2018; Linn et al., 2010; Charidimou et al., 2017; Charidimou et al., 2018).

To our knowledge, we are also the first to investigate absolute perfusion (with K_1; in mL/min/mL) and amyloid deposition in CAA, using ^{18}F-flutemetamol. Our analysis is in line with a recent study, in which a surrogate measure of cerebral perfusion was performed using SUVR analysis from an early phase (1–6 min) ^{11}C-PiB time frame, show-

ing reduced SUVR in patients with probable CAA against age-matched controls (Farid et al., 2015). Other recent studies showed higher amyloid load in cases with CAA versus controls with deep ICH using either ^{11}C-PiB (Tsai et al., 2017), or ^{18}F-florbetapir (Gurol et al., 2016; Raposo et al., 2017) amyloid ligands. Our results (Table 3) are comparable with a recent meta-analysis showing that the sensitivity and specificity of amyloid PET in detecting increased amyloid load in CAA was in the range 0.60–0.91 and 0.56–0.90, respectively (Charidimou et al., 2017). In our analysis, we demonstrated both differences in the ^{18}F-flutemetamol uptake, and impaired haemodynamics co-existing with amyloid burden in lobar ICH participants with probable CAA versus deep ICH patients (Tables 2-4, Fig. 7).

Previous studies examined associations between cerebral perfusion and hypo-metabolism in patients with dementia, using dual-tracer (amyloid ligand and ^{18}F-Fluorodeoxyglucose) protocols (Lin et al., 2016; Hsiao et al., 2012; Rodriguez-Vieitez et al., 2016; Rostomian et al., 2011; Meyer et al., 2011; Fu et al., 2014). In these studies, a surrogate SUVR measure of cerebral perfusion was typically extracted from early phase time frames ($\leq$ 1–6 min) of ^{18}F-florbetapir (Lin et al., 2016; Hsiao et al., 2012), or ^{11}C-PiB data (Rodriguez-Vieitez et al., 2016; Rostomian et al., 2011). In some cases, the SRTM-derived relative perfusion estimate (R_1) was assessed (Hsiao et al., 2012; Rodriguez-Vieitez et al., 2016; Meyer et al., 2011). Although all these studies showed strong correlations in the cerebral distribution of hypo-perfusion and hypo-metabolism versus cognitive mini mental state examination scores (Lin et al., 2016; Hsiao et al., 2012; Rodriguez-Vieitez et al., 2016; Rostomian et al., 2011; Meyer et al., 2011; Fu et al., 2014), weak or no associations between hypo-perfusion, amyloid load and cognitive scores were demonstrated in patients with dementia (Lin et al., 2016; Meyer et al., 2011; Fu et al., 2014). Furthermore, Lin et al. showed that in amnestic mild cognitive impairment, PET amyloid deposition occurs before the onset of perfusion deficits, and in AD, hypo-perfusion and amyloid load follow different spatial trajectories in the brain (Lin et al., 2016). It is known that the current amyloid PET tracers (including ^{18}F-flutemetamol) show high affinity to both parenchymal and perivascular β-amyloid (Ni et al., 2013). Hence, there is currently no PET diagnostic method for differentiating CAA from AD (Samarasekera et al., 2012; Charidimou et al., 2017; Charidimou et al., 2018; Farid et al., 2015). An interesting observation in our data analysis is that the perfusion estimate K_1 showed higher sensitivity and specificity versus the V_T in detecting cases with CAA versus patients with deep ICH. Although impaired resting perfusion may also be observed in cases of hypertension-related small vessel disease (which can lead to deep ICH) (Shi et al., 2016), our ROC results reflect the evident spatial extent of cerebral perfusion deficits in the presence of CAA. Demonstrating perfusion deficits and amyloid burden co-existing globally in non-demented cases with CAA is an important finding, as it can contribute towards elucidating the exact mechanisms of the presumed pathology (perivascular β-amyloid) against deep ICH, and can be considered as a diagnostic tool to potentially differentiate CAA against AD.

On ROC analysis, perfusion deficits and amyloid accumulation were congruent in cases with probable CAA (Fig. 7, Tables 3-4). These perfusion deficits and amyloid accumulation were both global within cases with probable CAA, which is consistent with the fact that CAA is a diffuse disease affecting globally the cerebral vasculature (Charidimou et al., 2018). It is known that up to about 20–30% of healthy elderly can be β-amyloid positive on amyloid-PET imaging, due to incipient AD (Charidimou et al., 2018; Mattsson et al., 2014; Bangen et al., 2017). Previous studies have reported perfusion decreases (Mattsson et al., 2014), increases (Bangen et al., 2017), or longitudinal increases and decreases (Sojkova et al., 2008) in certain brain regions (of β-amyloid positive healthy elderly) that are associated with the onset of AD. These conflicting perfusion results were attributed to either decreased brain function (reduced perfusion), or compensatory responses (increased perfusion) to incipient AD (Mattsson et al., 2014; Bangen et al., 2017;

Sojkova et al., 2008). On histopathology, patients with AD demonstrate a high prevalence of CAA which is usually mild to moderate, whilst in CAA with lobar ICH the underlying CAA pathology is severe (Charidimou et al., 2017; Charidimou et al., 2018). Following further assessments in larger patient cohorts, our imaging pattern can be important for the early diagnosis (before haemorrhage occurs) of severe CAA, against β-amyloid positive healthy elderly with incipient AD (Charidimou et al., 2017; Charidimou et al., 2018; Mattsson et al., 2014; Bangen et al., 2017; Sojkova et al., 2008). Moreover, our imaging pattern defines the framework to investigate whether mild to moderate CAA can be efficiently distinguished against β-amyloid positive healthy elderly with incipient AD.

4.2. Reduced versus full analysis

In the full interpolated and concatenated data analysis, all models identified perfusion deficits in cases with CAA versus patients with deep ICH. Unlike the 1-TC model, the diagnostic ability of the 2-TC model in detecting amyloid load was possibly compromised due to the 60 min interval between phases 1 and 2, in the interpolated data analysis. These results were similar in the concatenated data analysis, examined to assess whether the interpolated data component could bias model performance.

We showed that mIF 1-TC- and 2-TC-derived V_T from a 30 min PET-MR acquisition time can stratify brain areas with CAA vs deep ICH. These results were consistent with our visual assessments and SUVR analysis extracted from phase 2. Our reduced time SRTM analysis is in line with a previous PET-MR study, which showed that the SRTM-fitted parameter BP_{ND} is compromised when a 30 min is examined versus a 60 min (^{18}F-florbetapir) acquisition in normal ageing subjects (Scott et al., 2018). It is known that the K_1/k_2 ratio and the k_3-k_4 estimates used to measure V_T (1-TC-V_T=K_1/k_2; 2-TC-V_T=$K_1/k_2(1 + k_3/k_4)$) should be independent of the K_1 perfusion-dependant estimates alone (Gunn et al., 2001). As our K_1 (and k_2) estimates were significantly lower in cases with probable CAA versus patients with deep ICH for both 1-TC and 2-TC models (across all time frames analysed), our results indicate that our V_T estimates were independent of the K_1 estimates alone.

On AICc, all brain regions showed a marginal preference for 1-TC versus 2-TC in both full interpolated and reduced PET mIF analysis (supplementary file 5). This finding can indicate that either model can be used to describe ^{18}F-flutemetamol kinetics in our data. Since 2-TC involves additional fitted parameters versus 1-TC, a shorter interval between phases 1 and 2 may be needed to stabilise model fitting and potentially increase further its quality of fit and diagnostic ability. Heeman et al. recently showed that a dual-phase protocol (0–30 followed by a 90–110 min) may allow accurate estimation of SRTM-derived BP_{ND} when fitting SRTM-simulated ^{18}F-flutemetamol TACs (Heeman et al., 2019). However, they also showed systematic bias in SRTM-derived ^{18}F-flutemetamol uptake when fitting 2-TC-simulated TACs (Heeman et al., 2019). Although 2-TC and SRTM have both been used to describe ^{18}F-flutemetamol kinetics (Nelissen et al., 2009; Heurling et al., 2015), there is a clear discrepancy in their model architecture: the 2-TC describes the target tissue as having two-compartments, whilst the SRTM describes it as a single-compartment (such as the 1-TC; Fig. 1). Hence, based upon kinetic model principles, the 1-TC (not yet extensively investigated in terms of ^{18}F-flutemetamol uptake in the target tissue (Nelissen et al., 2009)) can also be used as a simplified approach to describe ^{18}F-flutemetamol kinetics, without introducing additional assumptions needed for SRTM (such as that non-specific binding is the same in the target and reference tissues) (Lammertsma and Hume, 1996; Lammertsma et al., 1996). Note that assessing model performance using synthetic PET data is beyond the scope of the current work, where we focused to assess whether mIF compartmental models can differentiate probable CAA patients from deep ICH patients.

4.3. Model based input function

In our mIF implementation, we adopted an alternative formulation of the standard kinetic model Fig. 1c, Eqs. (4) and (5). Previous model-based IF approaches in clinical data have mainly used the simultaneous estimation (SIME) approach, which attempts to estimate IF and kinetic parameters simultaneously from multiple brain regions (Zanotti-Fregonara et al., 2011; Zanderigo et al., 2015). However, this approach requires at least one blood sample to be acquired during PET imaging, and its test-retest reliability was recently found to be low (Zanderigo et al., 2018). Compared to previous model-based IF approaches, our mIF method did not require arterial sampling and can potentially be adapted to estimate metabolite corrected mIF using other PET tracers (considering that a small cohort pIF is available to estimate the $K_1\prime$ and $k_2\prime$).

4.4. Study limitations

Our 1-TC and 2-TC modelling assessments were derived from a small ICH cohort. However, this is the first study demonstrating congruent perfusion deficits and amyloid accumulation in a pilot cohort of cases with probable CAA versus patients with deep ICH. To calculate mIFs, we extracted mean pIF 1-TC model -derived $K_1\prime$ and $k_2\prime$ estimates and we also assumed a single compartment within the reference tissue (Eq. (4)). Our pIF was originally derived from a small cohort of three healthy controls and three AD patients from a previous ^{18}F-flutemetamol PET study (Nelissen et al., 2009; Heurling et al., 2015) and therefore may not be able to represent actual input functions for some patients. This can explain why pIF compartmental modelling did not detect differences in amyloid load between probable CAA and deep ICH. However, using mean pIF 1-TC model-derived $K_1\prime$ and $k_2\prime$ values, we aimed to avoid bias that could have been introduced in $K_1\prime$ and $k_2\prime$ values due to possible deviations of the pIF from the actual input functions, in some patients. Although it is standard for the cerebellum to be considered as a reference tissue devoid of ^{18}F-flutemetamol-specific receptors (Heurling et al., 2015), a single compartment may not always suffice in cases of slow non-specific retention (Nelissen et al., 2009). Hence, our mIF method will benefit from validation in a future experiment involving arterial sampling, to extensively assess the above assumptions. A small number of late arterial samples would be useful to scale our pIF on a per patient basis (Zanotti-Fregonara et al., 2013; Rissanen et al., 2015). A validation experiment would also give access to realistic patient-specific whole blood (non-metabolite corrected) curves, which may allow to reliably estimate the contribution of the fractional blood volume v_b in our mIF estimation and compartmental models (Lammertsma, 2002). The ideal reference standard for CAA diagnosis is a histopathological assessment, although this is rarely performed in living participants (Linn et al., 2010). Thus, we used the MR-based modified Boston criteria to classify lobar ICH participants with probable CAA versus deep ICH patients, as this is the current *in vivo* reference standard for diagnosing CAA (Linn et al., 2010; Charidimou et al., 2017; Charidimou et al., 2018). We showed that our mIF compartmental modelling reached high sensitivity and specificity in detecting perfusion deficits and amyloid load in CAA. We did not perform ^{15}O-water PET imaging to extract absolute blood flow quantification. Although we previously showed that the diagnostic performance of ^{15}O-water PET imaging depends on the quantification technique used, it is considered the reference standard imaging technique for perfusion assessments (Papanastasiou et al., 2018). Our model-derived K_1 alone demonstrated high sensitivity and specificity in detecting cases with CAA versus patients with deep ICH (across both 1-TC and 2-TC models). The 60 min interval between phases 1 and 2 possibly reduced the diagnostic ability of 2-TC in detecting amyloid load. The 60 min interval between phases 1 and 2 has also to some extent affected the discriminatory ability of mIF 1-TC and 2-TC modelling in the concatenated, compared to the interpolated data analysis used to stabilise model fitting (Table 2). A shorter interval may enhance the discriminatory ability of compartmental modelling in the concatenated data analysis and may therefore help to avoid interpolation between phases. In accordance with clinical practice, our imaging protocol was designed to reduce patient discomfort whilst accommodating additional patient scans in between phases 1 and 2.

5. Conclusions

The mIF 1-TC model method for ^{18}F-flutemetamol PET-MR showed the highest diagnostic ability in separately detecting impaired haemodynamics and amyloid load in probable CAA, versus deep ICH. We demonstrated that these findings can be reproduced using a reduced (30 min) PET acquisition, which is potentially useful for simplifying PET imaging protocols in the clinical setting compared to longer or dual-phase approaches.

Perfusion deficits and amyloid burden were congruent in ICH cases with probable CAA, therefore demonstrating a distinct imaging pattern which may have potential to be used as an important biomarker for the diagnosis of CAA. Our analysis can help to elucidate the mechanisms of perivascular amyloid deposition and can support further investigations for the early assessment of CAA.

Declaration of Competing Interest

None.

Supplementary materials

Supplementary material associated with this article can be found, in the online version, at doi:10.1016/j.neuroimage.2020.117482.

References

Ashburner, J., Friston, K.J, 2005. Unified segmentation. Neuroimage 26, 839–851.

Bangen, K.J., Clark, A.L., Edmonds, E.C., et al., 2017. Cerebral blood flow and amyloid-β Interact to affect memory performance in cognitively normal older adults. Front. Aging Neurosci. 9, 181.

Baron, J.C., Farid, K., Dolan, E., et al., 2014. Diagnostic utility of amyloid PET in cerebral amyloid angiopathy-related symptomatic intracerebral hemorrhage. J. Cereb. Blood Flow Metab. 34 (5), 753–758.

Boellaard, R., van Lingen, A., van Balen, S.C.M., Hoving, B.G., Lammertsma, A.A, 2001. Characteristics of a new fully programmable blood sampling device for monitoring blood radioactivity during PET. Eur. J. Nucl. Med. 28, 81–89.

Charidimou, A., Farid, K., Baron, J.C, 2017. Amyloid-PET in sporadic cerebral amyloid angiopathy: a diagnostic accuracy meta-analysis. Neurology 89 (14), 1490–1498.

Charidimou, A., Farid, K., Tsai, H.-.H., et al., 2018. Amyloid-PET burden and regional distribution in cerebral amyloid angiopathy: a systematic review and meta-analysis of biomarker performance. J. Neurol. Neurosurg. Psychiatry 89, 410–417.

Cunningham, V.J., Hume, S.P., Price, G.R., et al., 1991. Compartmental analysis of diprenorphine binding to opiate receptors in the rat in vivo and its comparison with equilibrium data in vitro. J. Cereb. Blood Flow Metab. 11, 1–9.

DeLong, E.R., DeLong, D.M., Clarke-Pearson, D.L, 1988. Comparing the areas under two or more correlated receiver operating characteristic curves: a nonparametric approach. Biometrics 44, 837–845.

Eriksson, L., Ingvar, M., Rosenqvist, G., Stone-Elander, S., Ekdahl, T., Kappel, P, 1995. Characteristics of a new automated blood sampling system for positron emission tomography. IEEE Trans. Nucl. Sci. 42, 1007–1011.

Farid, K., Hong, Y.T., Aigbirhio, F.I., et al., 2015. Early-phase 11C-PiB PET in amyloid angiopathy-related symptomatic cerebral hemorrhage: potential diagnostic value? PLoS ONE 10 (10), e0139926.

Fu, L., Liu, L., Zhang, J., Xu, B., Fan, Y., Tian, J, 2014. Comparison of dual-biomarker PIB-PET and dual-tracer PET in AD diagnosis. Eur. Radiol. 24, 2800–2809.

Gunn, R.N., Gunn, S.R., Cunningham, V.J, 2001. Positron emission tomography compartmental models. J. Cereb. Blood Flow Metab. 21, 635–652.

Gurol, M.E., Becker, J.A., Fotiadis, P., et al., 2016. Florbetapir-PET to diagnose cerebral amyloid angiopathy: a prospective study. Neurology 87 (19), 2043–2049.

Heeman, F., Yaqub, M., Lopes-Alves, I., et al., 2019. Optimized dual-time-window protocols for quantitative [^{18}F]flutemetamol and [^{18}F]florbetaben PET studies. Eur. J. Nucl. Med. Mol. Imaging Res. 9, 32.

Heurling, K., Buckley, C., Van Laere, K., Vandenberghe, R., Lubberink, M, 2015. Parametric imaging and quantitative analysis of the PET amyloid ligand [^{18}F]flutemetamol. Neuroimage 121, 184–192.

Hsiao, I.T., Huang, C.C., Hsieh, C.J., et al., 2012. Correlation of early-phase 18F-florbetapir (AV-45/Amyvid) PET images to FDG images: preliminary studies. Eur. J. Nucl. Med. Mol. Imaging 39, 613–620.

Klunk, W.E., Engler, H., Nordberg, A., et al., 2004. Imaging brain amyloid in Alzheimer's disease with Pittsburgh compound-B. Ann. Neurol. 55, 306–319.

Koopman, T., Verburg, N., Schuit, R.C., et al., 2018. Quantification of O-(2-[18F]fluoroethyl)-L-tyrosine kinetics in glioma. Eur. J. Nucl. Med. Mol. Imaging Res. 8, 72.

Lammertsma, A.A., Bench, C.J., Hume, S.P., et al., 1996. Comparison of methods for analysis of clinical [11C]raclopride studies. J. Cereb. Blood Flow Metab. 16, 42–52.

Lammertsma, A.A., Hume, S.P, 1996. Simplified reference tissue model for PET receptor studies. Neuroimage 4, 153–158.

Lammertsma, A.A, 2002. Radioligand studies: imaging and quantitative analysis. Eur. Neuropsychopharmacol. 12, 513–516.

Lin, K.J., Hsiao, I.T., Hsu, J.L., et al., 2016. Imaging characteristic of dual-phase 18F-florbetapir (AV-45/Amyvid) PET for the concomitant detection of perfusion deficits and beta-amyloid deposition in Alzheimer's disease and mild cognitive impairment. Eur. J. Nucl. Med. Mol. Imaging 43, 1304–1314.

Linn, J., Halpin, A., Demaerel, P., et al., 2010. Prevalence of superficial siderosis in patients with cerebral amyloid angiopathy. Neurology 74, 1346–1350.

Mattsson, N., Tosun, D., Insel, P.S., et al., 2014. Association of brain amyloid-beta with cerebral perfusion and structure in Alzheimer's disease and mild cognitive impairment. Brain 137 (5), 1550–1561.

Meyer, P.T., Hellwig, S., Amtage, F., et al., 2011. Dual-biomarker imaging of regional cerebral amyloid load and neuronal activity in dementia with PET and 11C-labeled Pittsburgh compound B. J. Nucl. Med. 52, 393–400.

Morris, E.D., Yoder, K.K., Wang, C., et al., 2005. ntPET: a new application of PET imaging for characterizing the kinetics of endogenous neurotransmitter release. Mol. Imaging 4, 473–489.

Nelissen, N., Van Laere, K., Thurfjell, L., et al., 2009. Phase 1 study of the Pittsburgh compound B derivative ^{18}F-flutemetamol in healthy volunteers and patients with probable Alzheimer disease. J. Nucl. Med. 50, 1251–1259.

Neuropathology Group, 2001. Medical research council cognitive function and aging study. Pathological correlates of late-onset dementia in a multicentre, community-based population in England and Wales. Neuropathology group of the medical research council cognitive function and ageing study (MRC CFAS). Lancet 357, 169–175.

Ni, R., Gillberg, P.G., Bergfors, A., Marutle, A., Nordberg, A, 2013. Amyloid tracers detect multiple binding sites in Alzheimer's disease brain tissue. Brain 136, 2217–2227.

Normandin, M.D., Morris, E.D, 2008. Estimating neurotransmitter kinetics with ntPET: a simulation study of temporal precision and effects of biased data. Neuroimage 39, 1162–1179.

Papanastasiou, G., Williams, M.C., Dweck, M.R., et al., 2018. Multimodality quantitative assessments of myocardial perfusion using dynamic contrast enhanced magnetic resonance and ^{15}O-labelled water positron emission tomography imaging. IEEE Trans. Radiat. Plasma Med. Sci. 2, 259–271.

Raposo, N., Planton, M., Péran, P., et al., 2017. Florbetapir imaging in cerebral amyloid angiopathy-related hemorrhages. Neurology 697–704.

Rissanen, E., Tuisku, J., Luoto, P., et al., 2015. Automated reference region extraction and population-based input function for brain [11C]TMSX PET image analyses. J. Cereb. Blood Flow Metab. 35 (1), 157–165.

Rodrigues, M.A., Samarasekera, N., Lerpiniere, C., et al., 2018. The Edinburgh CT and genetic diagnostic criteria for lobar intracerebral haemorrhage associated with cerebral amyloid angiopathy: model development and diagnostic test accuracy study. Lancet Neurol. 17, 232–240.

Rodriguez-Vieitez, E., Carter, S.F., Chiotis, K., et al., 2016. Comparison of early-phase 11C-deuterium-L-deprenyl and 11C-PiB PET for assessing brain perfusion in Alzheimer's disease. J. Nucl. Med. 57, 1071–1077.

Rostomian, A.H., Madison, C., Rabinovici, G.D., Jagust, W.J, 2011. Early 11C-PIB frames and 18F-FDG PET measures are comparable: a study validated in a cohort of AD and FTLD patients. J. Nucl. Med. 52, 173–179.

Samarasekera, N., Smith, C., Al-Shahi Salman, R, 2012. The association between cerebral amyloid angiopathy and intracerebral haemorrhage: systematic review and meta–analysis. J. Neurol. Neurosurg. Psychiatry 83, 275–281.

Scott, C.J., Jiao, J., Melbourne, A., et al., 2018. Reduced acquisition time PET pharmacokinetic modelling using simultaneous ASL–MRI: proof of concept. J. Cereb. Blood Flow Metab. 0 (00), 1–14.

Shi, Y., Thrippleton, M.J., Makin, S.D., et al., 2016. Cerebral blood flow in small vessel disease: a systematic review and meta-analysis. J. Cereb. Blood Flow Metab. 36 (10), 1653–1667.

Sojkova, J., Beason-Held, L., Zhou, Y., et al., 2008. Longitudinal cerebral blood flow and amyloid deposition: an emerging pattern? J. Nucl. Med. 49 (9), 1465–1471.

Tsai, H.H., Tsai, L.K., Chen, Y.F., et al., 2017. Correlation of cerebral microbleed distribution to amyloid burden in patients with primary intracerebral hemorrhage. Sci. Rep. 7, 44715.

Wolk, D.A., Price, J.C., Saxton, J.A., et al., 2009. Amyloid imaging in mild cognitive impairment subtypes. Ann. Neurol. 65, 557–568.

Wolk, D.A., Sadowsky, C., Safirstein, B., et al., 2018. Use of flutemetamol F 18-labeled positron emission tomography and other biomarkers to assess risk of clinical progression in patients with amnestic mild cognitive impairment. JAMA Neurol. 75, 1114–1123.

Zanderigo, F., D'Agostino, A.E., Joshi, N., et al., 2018. [^{11}C]Harmine binding to brain monoamine oxidase A:test-Retest properties and noninvasive quantification. Mol. Imaging Biol. 20, 667–681.

Zanderigo, F., Ogden, R.T., Parsey, R.V, 2015. Noninvasive blood-free full quantification of positron emission tomography radioligand binding. J. Cereb. Blood Flow Metab. 35, 148–156.

Zanotti-Fregonara, P., Chen, K., Liow, J.-.S., Fujita, M., Innis, R.B, 2011. Image-derived input function for brain PET studies: many challenges and few opportunities. J. Cereb. Blood Flow Metab. 31, 1986–1998.

Zanotti-Fregonara, P., Hirvonen, J., Lyoo, C.H., et al., 2013. Population-based input function modeling for [18F]FMPEP-d2, an inverse agonist radioligand for cannabinoid CB1 receptors: validation in clinical studies. PLoS ONE 8 (4), e60231.

Zwan, M.D., Bouwman, F.H., Konijnenberg, E., et al., 2017. Diagnostic impact of [18F]flutemetamol PET in early-onset dementia. Alzheimers Res. Ther. 9, 2.